

Multiscale model for phonon-assisted band-to-band tunneling in semiconductors

Arvind Ajoy,^{1, a)} S. E. Laux,^{2, b)} Kota V. R. M. Murali,^{3, c)} and Shreepad Karmalkar^{1, d)}

¹⁾ *Department of Electrical Engineering, Indian Institute of Technology Madras, Chennai 600036, India*

²⁾ *IBM T. J. Watson Research Center, Yorktown Heights, New York 10598, USA*

³⁾ *IBM Semiconductor Research and Development Center, Bangalore 560045, India*

(Dated: 28 August 2018)

We present a TCAD compatible multiscale model of phonon-assisted band-to-band tunneling (BTBT) in semiconductors, that incorporates the non-parabolic nature of complex bands within the bandgap of the material. This model is shown capture the measured current-voltage data in silicon, for current transport along the [100], [110] and [111] directions. Our model will be useful to predict band-to-band tunneling phenomena to quantify on and off currents in Tunnel FETs and in small geometry MOSFETs and FINFETs.

Keywords: Band-to-band tunneling, complex bandstructure, $sp^3d^5s^*$ tight binding method, energy dependent effective mass, transfer matrix method

I. INTRODUCTION

The on-current in Tunnel FETs and gate induced off-state drain current in small geometry MOSFETs are due to the tunneling of electrons between valence and conduction bands. This work deals with the process of phonon-assisted band-to-band tunneling (BTBT) across an indirect bandgap. One approach to compute phonon-assisted BTBT current is based on the Non-Equilibrium Green's function (NEGF) technique, for e.g. Refs. 1 and 2 using a basis of atomic orbitals. Electron transport is not ballistic, since scattering due to phonons is the driving force for BTBT current. The atomistic NEGF approach, though rigorous and accurate, requires the use of supercomputers³ to simulate realistically sized devices, especially when the effect of electron-phonon coupling⁴ is included. More efficient quantum transport algorithms such as the Wavefunction Method⁵ cannot be used since scattering is present. An alternate approach is to use the conventional drift-diffusion equations of semiconductor transport with a suitably calibrated model (eg. Refs. 6–8) describing the process of tunneling. Most commercially available semiconductor device simulators (TCAD) are based on this latter approach.

BTBT occurs via evanescent states corresponding to the conduction and valence bands. The properties of evanescent states are described by the complex bandstructure of the material. TCAD compatible models for BTBT in an indirect bandgap semiconductor^{9–13} use a simple parabolic approximation for the complex bandstructure within the bandgap, since the curvatures of the real and complex bands are identical at the band extrema^{14,15}. However, this approximation can introduce large errors in BTBT currents, since the tunneling

current depends exponentially on the action for tunneling, which in turn depends on the complex bandstructure over the entire bandgap, not merely at the band extrema (see Ref. 16 and Section IV). A first attempt to include the effect of non-parabolic complex bands to compute BTBT across an indirect bandgap⁷ ignored the role of phonons, and used the Esaki-Tsu formula¹⁷ meant for electron tunneling between conduction bands, leading to a prefactor which is independent of the valence band effective mass. We present a physically consistent, multiscale model that incorporates both the non-parabolicity of the complex bands and the physics of the electron-phonon interaction. The non-parabolicity is captured using energy dependent effective masses⁷, which connect a computation carried out on an atomistic scale (using an $sp^3d^5s^*$ tight binding scheme) with a tunneling model that is formulated using effective mass wave functions describing much larger length scales. Our model is symmetric with respect to the valence and conduction band parameters. This model can easily be implemented in a conventional TCAD tool. Finally, our model is shown to capture the measured current-voltage data¹⁸ in silicon for current transport along the [100], [110] and [111] directions.

This paper is organized as follows. In section II, we describe and derive the multiscale BTBT model. Section III compares the results of our model with experimental data. Section IV demonstrates the inadequacy of using a parabolic approximation to the complex bands while computing BTBT currents. Section V summarizes the important conclusions. Finally, the appendices provide supplementary information that will be useful to implement our model.

II. MODEL

Our approach is motivated by a combination of Refs. 7, 10, and 19. We restrict our attention to a 1-D problem. For definiteness, let x represent the transport di-

^{a)} arvindajoy@iitm.ac.in

^{b)} laux@us.ibm.com

^{c)} kotamurali@in.ibm.com

^{d)} karmal@ee.iitm.ac.in

rection. Then, in brief, Ref. 10 uses a simple WKB form ($\sim e^{\iota S(x)/\hbar}$, where the action $S(x)$ is correct up to $\mathcal{O}(\hbar^0)$) to describe the electronic wavefunctions within the bandgap, whereas Ref. 19 improves this description by including the first order term with respect to \hbar in $S(x)$. We include the idea of a position dependent effective mass from Ref. 7 in Ref. 19, and use a WKB form ($\sim (\partial E/\partial k)^{-1/2} e^{\iota S(x)/\hbar}$, with $\partial E/\partial k$ understood to be position dependent) appropriate to this situation²⁰. It is useful to note that this modified WKB form can be derived from a transfer matrix method²¹ by ignoring reflections. Finally, based on this insight, we use the transfer matrix method to correct for errors caused by the WKB based approach. Note that we do not consider the non-parabolic nature of real energy bands in this work. This allows a simple evaluation of integrals corresponding to the density of states involved in tunneling. We believe that this is a reasonable approximation while computing BTBT currents, since the density of states scales as $\sim \text{mass}^{1.5}$, unlike the tunneling probability which depends exponentially on the effective masses of the complex bands, via the action for tunneling.

We begin by extracting energy dependent effective masses $m_{VB}(E)$, $m_{CB}(E)$ of the imaginary parts of the valence and conduction bands from a computation^{22,23} of the direction-dependent complex bandstructure $k^{\parallel}(E; \mathbf{k}^{\perp})$ in an $sp^3d^5s^*$ tight binding scheme. The valence band maxima are assumed to be at $\mathbf{k} = \mathbf{0}$ to simplify the description that follows. Note that \mathbf{k}^{\parallel} is parallel or antiparallel to the transport direction, and \mathbf{k}^{\perp} is chosen by projecting the positions of all the conduction band valleys onto the $\mathbf{k}^{\parallel} = \mathbf{0}$ plane; k^{\parallel} is the magnitude of \mathbf{k}^{\parallel} . Note also that we have flipped the definitions of \perp and \parallel as used in Refs. 22 and 23, in order to remain consistent with Ref. 10. For each valence band, there are as many tunneling paths as there are conduction valleys, each tagged by a different value of \mathbf{k}^{\perp} . Within the bandgap $E_{VB\ max} < E < E_{CB\ min}$, we extract the masses using the definitions $\text{Im}[k^{\parallel}(E; \mathbf{0})] = \sqrt{2m_{VB}(E; \mathbf{0})(E - E_{VB\ max})}/\hbar$ and $\text{Im}[k^{\parallel}(E; \mathbf{k}^{\perp})] = \sqrt{2m_{CB}(E; \mathbf{k}^{\perp})(E_{CB\ min} - E)}/\hbar$ for the imaginary valence and complex conduction bands constituting a tunneling path. Near the band edges, the masses are extracted from the curvature of the bands.

Fig. 1 shows the energy band diagram of a p - n diode for a general case of non-uniform (and possibly degenerate) doping. We consider a large enough tunneling window so that tunneling current computed is independent of its extent. Following Ref. 10 (also see Table 1, Appendix A), the electronic wavefunction is written as $\psi(x, y, z) = u_x(x)u_y(y)u_z(z)$, where $u_y(y)$, $u_z(z)$ are plane waves with position-independent effective masses m_y , m_z . The extent of the device in y , z directions is denoted by l_y , l_z . An additional subscript v, c is used to denote quantities on the p , n sides of the junction respectively. Beyond the classical turning points ($x < a$, $x > b$), $u_x(x)$ is also assumed to be a plane wave. However, we modify the x dependent part of the wavefunctions (u_{vx} ,

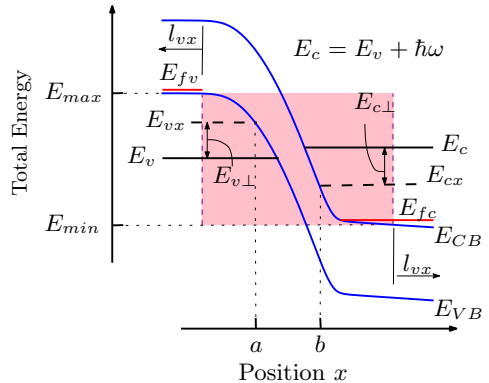


FIG. 1. Definition of quantities for BTBT model, following Refs. 10 and 19. The energies E_c , E_v as drawn demonstrate phonon absorption due to electron transfer from $v \rightarrow c$. The shaded region shows the tunneling window. The potential energy $U(x) \equiv E_{VB}(x)$.

u_{cx} for an electron in the valence and conduction bands respectively) within the region $a < x < b$ to include the effect of a position dependent effective mass and write

$$u_{vx}(x) = \sqrt{\frac{k_{vx} - k_{0vx}}{|\kappa_{vx}(x)|} \frac{m_{vx}(x)}{m_{vx}} \frac{\exp(\iota k_{0vx}(x-a))}{\sqrt{l_{vx}}}} \times \exp\left(-\int_a^x \kappa_{vx}(x') dx'\right) \quad (1a)$$

$$u_{cx}(x) = \sqrt{\frac{k_{cx} - k_{0cx}}{|\kappa_{cx}(x)|} \frac{m_{cx}(x)}{m_{cx}} \frac{\exp(\iota k_{0cx}(x-b))}{\sqrt{l_{cx}}}} \times \exp\left(-\int_x^b \kappa_{cx}(x') dx'\right) \quad (1b)$$

where $\kappa_{vx}(x) = \sqrt{2m_{vx}(x)(E_{vx} - U(x))/\hbar}$, and $\kappa_{cx}(x) = \sqrt{2m_{cx}(x)(E_g + U(x) - E_{cx})/\hbar}$. Here, k_{0vx} , k_{0cx} refer to the positions of the band extrema; l_{vx} , l_{cx} are the lengths of the regions outside the tunneling window on the p and n sides respectively (see Fig. 1); m_{vx} , m_{cx} are the effective masses at the band edges; and $m_{vx}(x)$, $m_{cx}(x)$ refer to the position dependent effective masses within the bandgap, obtained from $m_{VB}(E)$, $m_{CB}(E)$ respectively. The terms $k_{vx} - k_{0vx}$, $k_{cx} - k_{0cx}$ are understood to be evaluated at $x = a^-$ and $x = b^+$ respectively. Note that the products $m_{cx}m_{cy}m_{cz}$ and $m_{vx}m_{vy}m_{vz}$ remain invariant of the transport direction²⁴. We now follow the procedure used in Ref. 10. The essential differences are presented below. A detailed derivation is provided in Appendix B.

The combined wavefunction of the electron-phonon system is written as $|i\rangle = |\psi_i\rangle \cdot \dots n_{\mathbf{q},\mu}^i \dots$, where $i = c, v$ and $n_{\mathbf{q},\mu}^i$ gives the occupation number of the phonon mode μ with wavevector \mathbf{q} . The electron-phonon interaction Hamiltonian¹⁰ is

$$\mathcal{W}_{e-ph} = \sum_{\mathbf{q},\mu} \frac{M_{\mathbf{q},\mu}}{\sqrt{\Omega}} (a_{\mathbf{q},\mu} e^{\iota \mathbf{q} \cdot \mathbf{r}} + a_{\mathbf{q},\mu}^\dagger e^{-\iota \mathbf{q} \cdot \mathbf{r}}), \quad (2)$$

where $a_{\mathbf{q},\mu}^\dagger, a_{\mathbf{q},\mu}$ are phonon destruction, creation operators and $M_{\mathbf{q},\mu}$ is the strength of the electron-phonon interaction. From Ref. 25, $M_{\mathbf{q},\mu} = \sqrt{\frac{\hbar}{2\rho_s\omega_{\mathbf{q}}}}D_{\mathbf{q},\mu}$, where ρ_s is the density of the semiconductor, and $D_{\mathbf{q},\mu}$ is the intervalley deformation potential. $\hbar\omega_{\mathbf{q}}$ is energy of the phonon and Ω is the volume of the device $\approx (l_{cx}+l_{vx})l_y l_z$. There are four processes to be modeled in order to compute BTBT current – phonon emission or absorption (denoted e/a) driving the transfer of an electron either from the valence to the conduction band (denoted $v \rightarrow c$) or from the conduction to the valence band ($c \rightarrow v$). Since \mathcal{W}_{e-ph} is Hermitian, $|\langle c|\mathcal{W}_{e-ph}|v\rangle|^2 = |\langle v|\mathcal{W}_{e-ph}|c\rangle|^2$; i.e. given electronic states with energies E_v, E_c (that are assumed to be appropriately filled/empty to allow electron transfer) and phonon occupations $n_{\mathbf{q},\mu}^v, n_{\mathbf{q},\mu}^c$, the transfer $\{v \rightarrow c; e\}$ is equally likely as $\{c \rightarrow v; a\}$ within the framework of Fermi's golden rule. For want of a better alternative, we seek to replace the phonon occupation numbers by their expectation values given by the Bose-Einstein distribution. In doing so, it is important to recognize the subtle point that one cannot set both $n_{\mathbf{q},\mu}^v, n_{\mathbf{q},\mu}^c$ to be equal to $N_{\mathbf{q},\mu}$, the expectation value. We thus set $n_{\mathbf{q},\mu}^v = N_{\mathbf{q},\mu}$ for a $v \rightarrow c$ transfer and $n_{\mathbf{q},\mu}^c = N_{\mathbf{q},\mu}$ for a $c \rightarrow v$ transfer. The implicit assumption is that there exists a quick phonon relaxation process (not modeled by our Hamiltonian) that drives the phonon population to its equilibrium value after the electron transfer.

Consider first the processes $\{v \rightarrow c; e/a\}$. We then have the electron phonon interaction as

$$\overline{\langle c|\mathcal{W}_{e-ph}|v\rangle_{e/a}} = \sum_{q_x,\mu} \left[R_{e/a} \sqrt{N_{\mathbf{q},\mu} + \frac{1}{2} \pm \frac{1}{2}} \right]_{\#}, \quad (3a)$$

$$R_{e/a} = \frac{M_{\mathbf{q},\mu}}{\sqrt{\Omega}} \frac{1}{\sqrt{l_{cx}l_{vx}}} \times \int_a^b \sqrt{\alpha_c(x)\alpha_v(x)} e^{-\int_{e/a}(x)/\hbar} dx \quad (3b)$$

with

$$\begin{aligned} \int_{e/a}(x) &= \int_a^x \sqrt{2m_{vx}(x')(E_{vx} - U(x'))} dx' \\ &+ \int_x^b \sqrt{2m_{cx}(x')(E_g + U(x') - E_{cx})} dx' \quad (4a) \end{aligned}$$

$$Q_{e/a} = \hbar(\pm q_x + k_{0cx} - k_{0vx}), \quad (4b)$$

$$\alpha_c(x) = \frac{k_{cx} - k_{0cx}}{|\kappa_{cx}(x)|} \frac{m_{cx}(x)}{m_{cx}}, \quad (4c)$$

$$\alpha_v(x) = \frac{k_{vx} - k_{0vx}}{|\kappa_{vx}(x)|} \frac{m_{vx}(x)}{m_{vx}} \quad \text{and} \quad (4d)$$

$$N_{\mathbf{q},\mu} = \frac{1}{\exp(\hbar\omega_{\mathbf{q},\mu})/k_B T} - 1. \quad (4e)$$

The overbar in eq. (3) indicates the use of the expectation value $N_{\mathbf{q},\mu}$ for the phonon occupation number. The

$\#$ in eq. (3) specifies the condition $q_y = \pm(k_{vy} - k_{cy})$, $q_z = \pm(k_{vz} - k_{cz})$. This condition is obtained from the fact for example that $\int \exp(\iota(q_y - (k_{cy} - k_{vy}))) dy = l_y \delta_{q_y, k_{cy} - k_{vy}}$ and the assumption that $M_{\mathbf{q},\mu}$ is weakly dependent on \mathbf{q} . The upper (lower) sign in \pm in eqs. (3), (4) corresponds to the first (second) process in e/a (i.e. phonon emission/absorption) in the transfer of an electron from the valence band to the conduction band.

The integral involving $e^{-\int_{e/a}(x)}$ is next evaluated using the saddle point method. Extending x to the complex plane w , we have

$$R_{e/a} = \frac{M_{\mathbf{q},\mu}}{\sqrt{\Omega}} \sqrt{\frac{2\pi\hbar}{l_{cx}l_{vx}}} \frac{\sqrt{\alpha_c(w_\sigma)\alpha_v(w_\sigma)}}{\sqrt{\left| \frac{d^2 \int_{e/a}(w_\sigma)}{dw^2} \right|}} \exp\left(-\frac{\int_{e/a}(w_\sigma)}{\hbar}\right) \quad (5)$$

with $\frac{d \int_{e/a}(w_\sigma)}{dw} = 0$. The prefactor $\sqrt{\alpha_c(x)\alpha_v(x)}$ in the integral is approximated with its value at the saddle point.

Next consider the processes $\{c \rightarrow v; e/a\}$, leading to

$$\overline{\langle v|\mathcal{W}_{e-ph}|c\rangle_{e/a}} = \sum_{q_x,\mu} \left[R'_{e/a} \sqrt{N_{\mathbf{q},\mu} + \frac{1}{2} \pm \frac{1}{2}} \right]_{\#'} \quad (6)$$

The $'$ denotes the reversal of the transfer direction. $\#'$ implies $q_y = \mp(k_{vy} - k_{cy})$, $q_z = \mp(k_{vz} - k_{cz})$. Using the Hermiticity of \mathcal{W}_{e-ph} , we can show that $|R_{e/a}| = |R'_{e/a}|$ for a given pair of energies E_v, E_c and phonon energy $\omega_{\mathbf{q},\mu}$. This relationship allows us to describe all the four processes in terms of quantities derived for the two $\{v \rightarrow c; e/a\}$ processes.

We now derive the net number of electrons, N_t , transferred per unit time from $v \rightarrow c$ (including spin) using Fermi's golden rule. As mentioned earlier, each pair of intersecting complex valence and conduction bands constitutes a tunneling path. Based on the symmetry of the crystal, there can be a multiplicity of ν_p different values of \mathbf{k}^\parallel within the first Brillouin zone (and hence ν_p tunneling paths) that give the same complex bands $k^\perp(E; \mathbf{k}^\parallel)$ (see Appendix C). Denoting $R_{e/a}$ evaluated in eq. (5) along tunneling path p as $R_{e/a,p}$, we have

$$\begin{aligned} N_t &= 2 \sum_p \sum_{\substack{k_{vx}, k_{vy}, k_{vz} \\ k_{cx}, k_{cy}, k_{cz}}} \sum_{q_x,\mu} \sum_{e/a} \nu_p \frac{2\pi}{\hbar} \left| R_{e/a,p} \right|_{\#}^2 \times \\ &\left[\left(N_{\mathbf{q},\mu} + \frac{1}{2} \pm \frac{1}{2} \right)_{\#} \times f_v(E_v)(1 - f_c(E_c)) \right. \\ &\left. - \left(N_{\mathbf{q},\mu} + \frac{1}{2} \mp \frac{1}{2} \right)_{\#} \times f_c(E_c)(1 - f_v(E_v)) \right] \times \\ &\left[\delta(E_c \pm \hbar\omega_{\mathbf{q},\mu} - E_v) \right]_{\#}. \quad (7) \end{aligned}$$

where $f_v(E_v), f_c(E_c)$ are the Fermi functions evaluated on the two sides. As described in Appendix B, the current density $J = -eN_t/l_y l_z$ is then

$$\begin{aligned}
J = & \sum_p \frac{eV_p}{2^{2.25}\pi^{2.5}\hbar^{8.5}} \sqrt{m_{cy}^p m_{cz}^p m_{vy}^p m_{vz}^p} \\
& \times \sum_{\mu, e/a} \frac{(m_{cx}^p(x_0^p) m_{vx}^p(x_0^p))^{1.25}}{(m_{cx}^p(x_0^p) + m_{vx}^p(x_0^p))^{0.75}} \frac{(E_g \pm \hbar\omega)^{0.25}}{|\kappa_{cx}(x_0^p) \kappa_{vx}(x_0^p)|} [M_{\mathbf{q}, \mu}^2]_* \left[-\frac{dU}{dx} \right]_{x_0}^{-0.5} \\
& \times \int_{E_{min} \pm \hbar\omega}^{E_{max}} dE_{vx} T(E_{vx}) \left[\bar{E}_\perp^2 - \bar{E}_\perp (\bar{E}_\perp + E_{vx} \mp \hbar\omega - E_{min}) e^{-(E_{vx} \mp \hbar\omega - E_{min})/\bar{E}_\perp} \right] \times \\
& \left[\left(N_{\mathbf{q}, \mu} + \frac{1}{2} \pm \frac{1}{2} \right)_* \times f_v(E_{vx}) (1 - f_c(E_{vx} \mp \hbar\omega)) \right. \\
& \left. - \left(N_{\mathbf{q}, \mu} + \frac{1}{2} \mp \frac{1}{2} \right)_* \times f_c(E_{vx} \mp \hbar\omega) (1 - f_v(E_{vx})) \right], \tag{8}
\end{aligned}$$

with $T(E_{vx}) = e^{-\Lambda}$,

$$\begin{aligned}
\Lambda = & \frac{2}{\hbar} \left[\int_a^{x_0^p} \sqrt{2m_{vx}^p(x') (E_{vx} - U(x'))} dx' \right. \\
& \left. + \int_{x_0^p}^{b_0} \sqrt{2m_{cx}^p(x') (E_g \pm \hbar\omega - (E_{vx} - U(x')))} dx' \right], \tag{9a}
\end{aligned}$$

where the crossover point x_0^p is a solution of

$$\frac{m_{vx}^p(x_0^p)}{m_{cx}^p(x_0^p)} = \frac{(E_g \pm \hbar\omega - (E_{vx} - U(x_0^p)))}{(E_{vx} - U(x_0^p))}, \tag{9b}$$

and $U(b_0) = E_{vx} - (E_g \pm \hbar\omega)$. The scaling factor

$$\bar{E}_\perp = \hbar \int_{x_0^p}^{b_0} \sqrt{\frac{2m_{cx}(x')}{E_g \pm \hbar\omega - (E_{vx} - U(x'))}} dx' \tag{9c}$$

and the $*$ refers to the condition $q_x = \pm(k_{0vx}^p - k_{0cx}^p)$, $q_y = \pm(k_{0vy}^p - k_{0cy}^p)$, $q_z = \pm(k_{0vz}^p - k_{0cz}^p)$. The effective masses $m_{cx}^p(x_0^p)$, $m_{vx}^p(x_0^p)$ and the wavevectors $\kappa_{cx}^p(x_0^p)$, $\kappa_{vx}^p(x_0^p)$ are obtained from the complex bandstructure of the material. Note that we have used ω to mean $\omega_{\mathbf{q}, \mu}|_*$ in order to avoid tedious notation.

The expression in eq. (8) is symmetric with respect to the conduction and valence band masses. The term $T(E_{vx}) = e^{-\Lambda}$ is independent of $E_{c\perp}$, $E_{v\perp}$ and is similar in spirit to the transmission coefficient $T(E_x)$ computed with a transfer matrix method in Ref. 7. To correct for errors introduced by neglecting reflections²¹ in assuming the WKB forms eq. (1a) and eq. (1b), we use the transfer matrix method to compute the term equivalent to $T(E_{vx})$. We also include the velocity ratio $(k_{cx} - k_{0cx})m_{vx}/(k_{vx} - k_{0vx})m_{cx}$ in the formula for T . We find that the inclusion of the transfer matrix method changes the current by a factor approximately between 1 – 2 (see Appendix D). The deviation between a WKB

calculation and more accurate computational methods is known to be dependent on doping (and hence electric field). A similar trend of WKB underestimating the tunneling probability, as observed here, has been reported in Ref. 26 (in the case of BTBT in a direct bandgap material for moderate doping, see Fig. 6(c) therein) and Ref. 27 (in the case of tunneling through a triangular barrier).

III. RESULTS

We now test our model against experimental data¹⁸ available for BTBT in silicon. This data is unique in that the same doping profile has been used to study BTBT along the [100], [110] and [111] directions. We implement our model in the open source drift-diffusion based

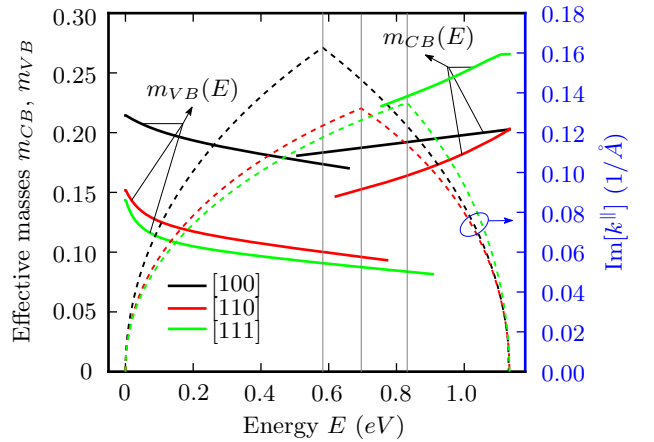


FIG. 2. Effective masses m_{CB} , m_{VB} (solid lines) and imaginary wavevectors $\text{Im}[k^{\parallel}]$ (dashed lines) corresponding to the tunneling path that minimizes area $\int_{E_g} \text{Im}[k^{\parallel}(E)] dE$ bounded by the imaginary parts of the valence and conduction bands, in silicon along the [100], [110] and [111] directions.

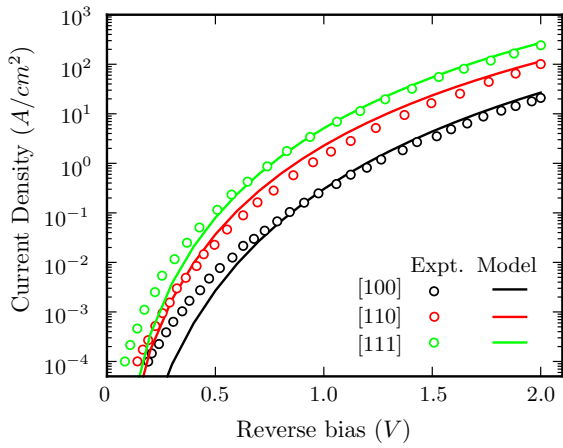


FIG. 3. Comparison between our model and experimental data (doping $Q2$ of Ref. 18). Note that the term $T(E_{vx})$ in eq. (8) has been computed using transfer matrices.

TCAD code *pyEDA*²⁸. We also modify the *pyEDA* code to include the effects of degenerate doping and incomplete ionization of dopants. Information regarding the phonon energies, modes and electron-phonon deformation potentials are taken from Ref. 29. Owing to the conservation condition $*$ in eq. (8), we only require the phonon modes along the $\Delta \equiv \Gamma - X$ direction in silicon. To summarize, there is one longitudinal optical (LO) and acoustic (LA) mode, and two doubly degenerate transverse optical (TO) and acoustic (TA) phonon modes with energies 61.2, 47.4, 59.0, 19.0 meV and deformation potentials 6.0, 5.9, 6.0, 5.9×10^8 eV/cm respectively. The density $\rho_s = 2.328$ g/cm³ is taken from Ref. 25. The TA mode provides the largest contribution to the BTBT current (for example, $\approx 83\%$ of the total current at reverse bias of 2.0 V for the [110] direction in the device considered here.) In order to simplify computation, we restrict ourselves to the ν tunneling paths (and hence values of \mathbf{k}^\perp) that minimize the area $\int_{E_g} \text{Im}[k^\parallel(E)]dE$ bounded by the imaginary parts of the valence and conduction bands involved in tunneling. Other tunneling paths enclose much larger areas and are hence expected to contribute negligibly to tunneling current, due to the term e^{-A} in eq. (8). Further, these ν paths all happen to originate from the valence band for light holes. The multiplicity $\nu = 4, 2, 6$ for transport along the [100], [110] and [111] directions respectively (Appendix C) in silicon. Fig. 2 shows the energy dependent effective mass computed using an $sp^3d^5s^*$ tight binding scheme²² and parameters from Ref. 30. The invariant product $m_{cx}m_{cy}m_{cz}$ is $0.891m_0 \times 0.201m_0 \times 0.201m_0$, written using a coordinate system aligned with the major and minor axes of any one of the six conduction band ellipsoids. Similarly, the product $m_{vx}m_{vy}m_{vz}$ is $0.214m_0 \times 0.152m_0 \times 0.144m_0$, corresponding to the effective masses of the light holes $m_{lh,[100]}$, $m_{lh,[110]}$ and $m_{lh,[111]}$ along the three orthogonal [100], [110] and [111] directions respectively. The value of $m_{cy}m_{cz}$ and $m_{vy}m_{vz}$ in eq. (8) are obtained

from these invariant products and the values of m_{cx} , m_{vx} in Fig. 2 at the band edges. Fig. 3 shows that the results of our model agree very well with the experimental data. We have assumed a bandgap $E_g = 0.92$ eV, corresponding to a bandgap narrowing of ~ 0.2 eV, by fitting the results of our model with the experimental data (We found this to be a better strategy than calculating the bandgap narrowing a priori, since the value of bandgap narrowing is dependent on doping, which is non-uniform for the devices we have considered here. The model for BTBT that we have derived assumes a uniform bandgap.) This value of narrowing is consistent with studies on bandgap narrowing in space charge regions^{31,32} for the doping levels considered here. Further, based on a result obtained using $\mathbf{k} \cdot \mathbf{p}$ theory³³ that $m \propto E_g$, we have scaled all the effective masses by the factor E_g/E_{g0} , where E_{g0} is the bandgap for moderate doping. At low values of reverse bias, our model underestimates the experimentally observed value of current (for e.g., for transport along [100], at $V_{bias} = 0.25$ V, $I_{expt.} \approx 3 \times 10^{-4}$ A/cm² whereas $I_{model} \approx 4.7 \times 10^{-5}$ A/cm²). It is likely that some other mechanism of current transport (such as tunneling via traps, or SRH recombination via traps) could possibly explain the difference between our simulations and experimental data at small values of reverse bias (see for e.g. Fig. 7 of Ref. 12). It is possible that the trap distribution/energies are different in the experimental samples that we have compared our model against for transport along the different directions, leading to a better match between the experimental data and the model for the [110] direction. A detailed analysis of this deviation could be the focus of future work.

IV. ERROR DUE TO PARABOLIC APPROXIMATION OF COMPLEX BANDS

We now demonstrate the inadequacy of using a parabolic approximation to the complex bandstructure while computing BTBT currents. Fig. 4(a) shows a parabolic approximation (dashed lines) to the complex bands (solid lines, obtained from an $sp^3d^5s^*$ calculation) along the tunneling path that minimizes $A = \int_{E_g} \text{Im}[k^\parallel(E)]dE$. The curvatures of the imaginary and real bands are identical at the band extrema. The values of m_l , m_t and m_{lh} are from Ref. 30. The expressions for m_{le} are from Ref. 7, based on the theory in Ref. 24. The areas A in the $sp^3d^5s^*$ method and parabolic approximations are listed in Fig. 4(b); the errors due to a parabolic approximation with respect to the $sp^3d^5s^*$ results are indicated in Fig. 4(a). Note that the error is largest along the [111] direction. A simple result for the transmission (setting the phonon energy to 0, assuming a uniform field F , and using a WKB approximation) gives¹⁶ $T = \nu e^{-2A/eF}$, where ν is the multiplicity of tunneling paths. As indicated in Fig. 4(b), the parabolic approximation underestimates the tunneling current by a factor of 44.3 along the [111] direction. Finally, Fig. 4(c) shows

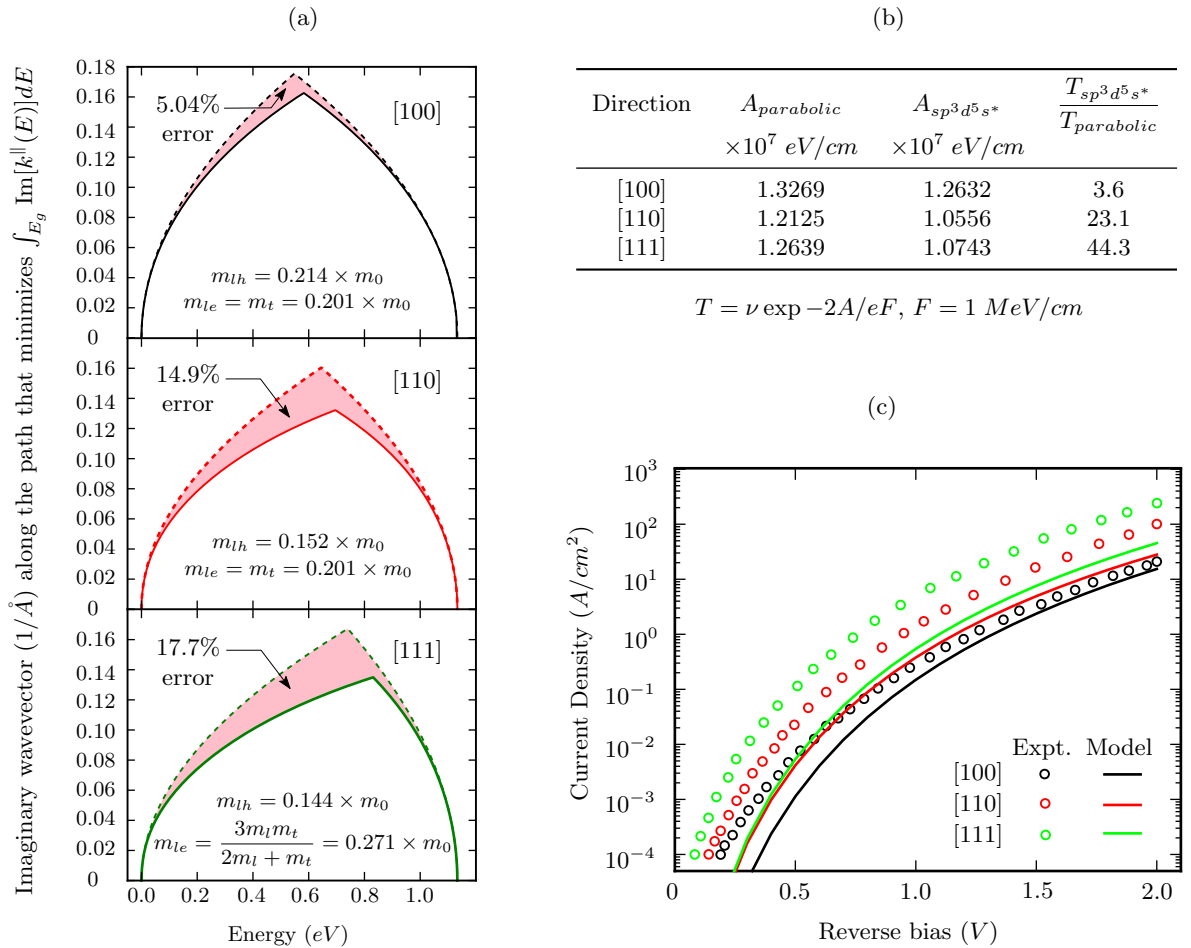


FIG. 4. (a) Parabolic approximation (dashed) to complex bands (solid) showing the errors in estimating $A = \int_{E_g} \text{Im}[k^{\parallel}(E)]dE$. (b) Comparison of results for the case of a uniform field F using a simple WKB expression (c) Comparison of results using our BTBT model for parabolic complex bands. Note that we use the TM method with the same bandgap (and scaling of masses) as in Fig. 3.

the results of using the parabolic approximation in our BTBT model (as usual, $T(E_{vx})$ is computed using transfer matrices). We use the same bandgap (and scaling of masses) as in Fig. 3. Clearly, the parabolic approximation does not capture the measured data. Further, it significantly underestimates the difference between the currents in the [111] and [100] directions. We would like to clarify that though the choice of effective energy gap can increase or decrease the absolute values of the current levels, it cannot correctly predict the difference in currents between the [111] and [100] directions. This can be seen from Fig. 4(a), where error in the action for tunneling along the [111] direction is significantly greater than that along the [100] direction.

V. CONCLUSION

In conclusion, we have presented a multiscale model for phonon assisted BTBT that accounts for the complex

bandstructure within the bandgap of an indirect semiconductor. We have shown that the predictions of this model compare very well with experimental data for BTBT in silicon along different orientations. We have shown that including the effect of non-parabolic complex bands is important to capture the correct difference between tunneling currents observed along the [100], [110] and [111] directions. The framework presented here can be used to modify Tanaka's results¹⁰ on BTBT across a direct bandgap to include the effect of an energy dependent effective mass. Such an extension will find application in treating BTBT in materials such as germanium, where the direct bandgap is only about 0.15 eV larger than the indirect bandgap.

Appendix A: Description of wavefunctions and energies

The wavefunctions within the effective mass approximation are written as $\Psi_v(x, y, z) = u_{vx}(x)u_{vy}(y)u_{vz}(z)$

TABLE I. Description of wavefunctions assumed, following Ref. 10.

Region	Wavefunction	Energy
	$\psi_v(x, y, z) = u_{vx}(x)u_{vy}(y)u_{vz}(z)$	$E_v = E_{vx} - E_{v\perp}$
	$-\infty < x < b$ $u_{vy}(y) = e^{ik_{vy}y}/\sqrt{l_y}$, $u_{vz}(z) = e^{ik_{vz}z}/\sqrt{l_z}$	$E_{v\perp} = \hbar^2(k_{vy} - k_{0vy})^2/2m_{vy} + \hbar^2(k_{vz} - k_{0vz})^2/2m_{vz}$
VB	$-\infty < x < a$ $u_{vx}(x) = e^{ik_{vx}(x-a)}/\sqrt{l_{vx}}$	$E_{vx} = E_{max} - \hbar^2(k_{vx} - k_{0vx})^2/2m_{vx}$
	$a < x < b$ $u_{vx}(x)$ — eq. (1a)	$\left[-\frac{\hbar^2}{2m_{vx}} \left(-\iota \frac{d}{dx} - k_{0vx} \right)^2 + U(x) \right] u_{vx}(x) = E_{vx} u_{vx}(x)$
	$\psi_c(x, y, z) = u_{cx}(x)u_{cy}(y)u_{cz}(z)$	$E_c = E_{cx} + E_{c\perp}$
	$a < x < \infty$ $u_{cy}(y) = e^{ik_{cy}y}/\sqrt{l_y}$, $u_{cz}(z) = e^{ik_{cz}z}/\sqrt{l_z}$	$E_{c\perp} = \hbar^2(k_{cy} - k_{0cy})^2/2m_{cy} + \hbar^2(k_{cz} - k_{0cz})^2/2m_{cz}$
CB	$a < x < b$ $u_{cx}(x)$ — eq. (1b)	$\left[\frac{\hbar^2}{2m_{cx}} \left(-\iota \frac{d}{dx} - k_{0cx} \right)^2 + E_g + U(x) \right] u_{cx}(x) = E_{cx} u_{cx}(x)$
	$b < x < \infty$ $u_{cx}(x) = e^{ik_{cx}(x-b)}/\sqrt{l_{cx}}$	$E_{cx} = E_{min} + \hbar^2(k_{cx} - k_{0cx})^2/2m_{cx}$

and $\Psi_c(x, y, z) = u_{cx}(x)u_{cy}(y)u_{cz}(z)$ for an electron in the valence and conduction bands respectively. The extents of the device in the y, z directions are l_y, l_z . As shown in Fig. 1, the component of the energy of an electron corresponding to its motion in the yz plane is designated $E_{v\perp}$ in the valence band and $E_{c\perp}$ in the conduction band. Note that $E_{v\perp}, E_{c\perp} \geq 0$.

Further, following Ref. 10, u_{vy}, u_{cy} and u_{vz}, u_{cz} are plane waves. On the other hand, u_{vx} and u_{cx} are assumed to be plane waves outside the classical turning points (i.e. $x < a$ and $x > b$). This corresponds to making the approximation (see Fig. 1(b) of Ref. 10) that the energy bands are flat until $x = a^-$ (with the valence band edge at E_{max}) and beyond $x = b^+$ (with the conduction band edge at E_{min}). Table I summarizes the expressions for the wavefunctions and energies in different regions.

Appendix B: Derivation of tunneling current

The summations in eq. (7) are first converted into integrals, for e.g. $\sum_{k_{cx}} \rightarrow \frac{l_{cx}}{2\pi} \int dk_{cx}$, $\sum_{k_{cy}} \rightarrow \frac{l_y}{2\pi} \int dk_{cy}$. Further, the integrals are rewritten in terms of energies using the relationship between k and E outside the region of tunneling, for e.g. $\int dk_{cx} = \frac{m_{cx}}{\sqrt{2\hbar}} \int \frac{dE_{cx}}{\sqrt{E_{cx}}}$, $\int dk_{cy} dk_{cz} = \frac{2\pi\sqrt{m_{cy}m_{cz}}}{\hbar^2} \int dE_{c\perp}$. In order to determine the limits of integration, we impose the conditions that $E_c \geq E_{min}$ and $E_v \leq E_{max}$. By definition, $E_c, E_v \geq 0$. Anticipating the physical reality that tunneling will be dominated by states with $E_{\perp} = E_{c\perp} + E_{v\perp} \rightarrow 0$, we also impose conditions that $E_{cx} \geq E_{min}$ and $E_{vx} \leq E_{max}$. This gives the limits of integration. The current density $J = -eN_t/l_y l_z$ is

$$\begin{aligned}
J = & \sum_p \frac{eV_p}{4\pi^3 \hbar^8} \sqrt{m_{cy}^p m_{cz}^p m_{vy}^p m_{vz}^p} \sum_{\mu, e/a} \frac{m_{cx}^p(w_{\sigma}^p) m_{vx}^p(w_{\sigma}^p)}{|\kappa_{cx}^p(w_{\sigma}^p) \kappa_{vx}^p(w_{\sigma}^p)|} \int dq_x \int_{E_{min} \pm \hbar\omega}^{E_{max}} dE_{vx} \int_0^{E_{vx} \mp \hbar\omega - E_{min}} dE_{v\perp} \int_0^{E_{max} \mp \hbar\omega - E_{min}} dE_{c\perp} \\
& \times \int_{E_{min}}^{E_{max} \mp \hbar\omega - E_{c\perp}} dE_{cx} [M_{\mathbf{q}, \mu}^2]_{\#} \left| \frac{d^2 f_{e/a}(w_{\sigma}^p)}{dw^2} \right|^{-1} \left| \exp\left(-\frac{2f_{e/a}(w_{\sigma}^p)}{\hbar}\right) \right| \delta(E_{cx} - (E_{vx} \mp \hbar\omega - E_{c\perp} - E_{v\perp})) \\
& \times \left[\left(N_{\mathbf{q}, \mu} + \frac{1}{2} \pm \frac{1}{2} \right)_{\#} f_v(E_{vx} - E_{v\perp})(1 - f_c(E_{cx} + E_{c\perp})) - \left(N_{\mathbf{q}, \mu} + \frac{1}{2} \mp \frac{1}{2} \right)_{\#} f_c(E_{cx} + E_{c\perp})(1 - f_v(E_{vx} - E_{v\perp})) \right]
\end{aligned} \tag{B1}$$

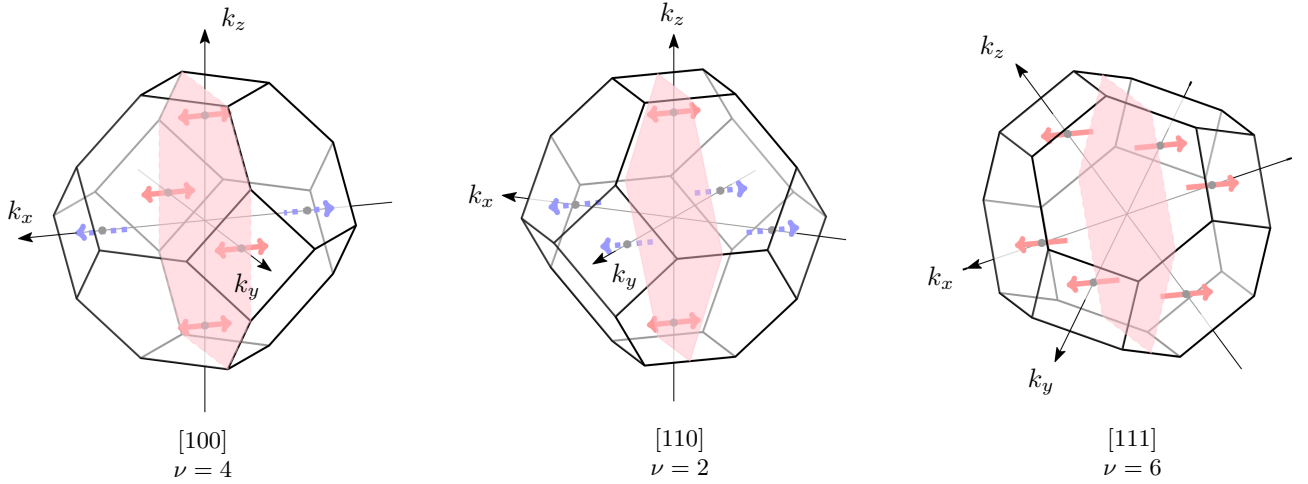


FIG. 5. Multiplicity ν of tunneling paths in silicon along the [100], [110] and [111] directions. The plane $\mathbf{k}^{\parallel} = \mathbf{0}$ is shown shaded. The red (solid) paths provide a higher tunneling probability than the blue (dashed) paths.

where the summation over q_x has also been converted to an integral. E_{cx} is eliminated from eq. (B1) due to the delta function. Further simplification requires making the assumption that only states with small values of $E_{c\perp}$, $E_{v\perp}$ and hence $E_{\perp} = E_{c\perp} + E_{v\perp}$ contribute significantly to tunneling. Tanaka¹⁰ approximates an integral of the form $\int_0^{X_0} \int_0^{Y_0} F(X+Y) dX dY \approx \int_0^{Y_0} V F(V) dV$ where $V = X+Y$ (and $X \equiv E_{c\perp}$, $Y \equiv E_{v\perp}$) for the case that $F(V)$ is significant only for small V . However, Tanaka's expressions do not include the Fermi functions as in eq. (B1). We drop $E_{v\perp}$ in the arguments of the Fermi functions f_c, f_v and write

$$\begin{aligned}
 J = & \sum_p \frac{e\nu_p}{4\pi^3\hbar^8} \sqrt{m_{cy}^p m_{cz}^p m_{vy}^p m_{vz}^p} \sum_{\mu, e/a} \frac{m_{cx}^p(w_{\sigma}^p) m_{vx}^p(w_{\sigma}^p)}{|\kappa_{cx}^p(w_{\sigma}^p) \kappa_{vx}^p(w_{\sigma}^p)|} \\
 & \times \int dq_x \int_{E_{min} \pm \hbar\omega}^{E_{max}} dE_{vx} \int_0^{E_{vx} \mp \hbar\omega - E_{min}} E_{\perp} dE_{\perp} \\
 & \times [M_{\mathbf{q}, \mu}^2]_{\#} \left| \frac{d^2 f_{e/a}(w_{\sigma}^p)}{dw^2} \right|^{-1} \left| \exp\left(-\frac{2f_{e/a}(w_{\sigma}^p)}{\hbar}\right) \right| \\
 & \times \left[\left(N_{\mathbf{q}, \mu} + \frac{1}{2} \pm \frac{1}{2} \right)_{\#} \times f_v(E_{vx})(1 - f_c(E_{vx} \mp \hbar\omega)) \right. \\
 & \left. - \left(N_{\mathbf{q}, \mu} + \frac{1}{2} \mp \frac{1}{2} \right)_{\#} \times f_c(E_{vx} \mp \hbar\omega)(1 - f_v(E_{vx})) \right]. \quad (B2)
 \end{aligned}$$

Finally, following Ref. 10, w_{σ}^p and hence $f_{e/a}(w_{\sigma}^p)$ are functions of $Q_{e/a}, E_{\perp}$. We expect that the dominant contribution to tunneling will be for $Q_{e/a} = 0, E_{\perp} = 0$. We

thus expand $f_{e/a}(w_{\sigma}^p)$ using a Taylor approximation

$$\begin{aligned}
 f_{e/a}(w_{\sigma}^p) \equiv f_{e/a}(Q_{e/a}, E_{\perp}) = & f_{e/a}(0, 0) + \frac{\partial f_{e/a}(0, 0)}{\partial Q_{e/a}} Q_{e/a} \\
 & + \frac{1}{2} \frac{\partial^2 f_{e/a}(0, 0)}{\partial Q_{e/a}^2} Q_{e/a}^2 + \frac{\partial f_{e/a}(0, 0)}{\partial E_{\perp}} E_{\perp}. \quad (B3)
 \end{aligned}$$

To determine the coefficients in the above equation, we make the approximation that $m_{cx}^p(x), m_{vx}^p(x)$ are gently varying functions of x , and hence ignore their spatial derivatives. This allows reuse of many of the expressions derived in Ref. 10 with minor modifications. Then $x_0^p = w_{\sigma}^p(0, 0)$ is a solution of the equation

$$\begin{aligned}
 & \sqrt{2m_{vx}^p(x)(E_{vx} - U(x_0^p))} = \\
 & \sqrt{2m_{cx}^p(x)(E_g \pm \hbar\omega - (E_{vx} - U(x_0^p)))} \quad (B4a)
 \end{aligned}$$

and represents the point of intersection of the imaginary parts of the complex valence and conduction bands. We have

$$\Lambda = \frac{2f_{e/a}(0, 0)}{\hbar} \quad (B4b)$$

which gives eq. (9a). The coefficient $\frac{\partial f_{e/a}(0, 0)}{\partial Q_{e/a}} = \iota x_0^p$ is purely imaginary and hence can be ignored. Further,

$$\frac{\partial^2 f_{e/a}(0, 0)}{\partial Q_{e/a}^2} = 2 \frac{\sqrt{2m_{rx_0}(E_g \pm \hbar\omega)}}{m_{cx}^p(x_0^p) + m_{vx}^p(x_0^p)} \left/ \left[-\frac{dU}{dx} \right]_{x_0^p} \right. \quad (B4c)$$

where m_{rx_0} is a reduced mass given by

$$m_{rx_0} = \frac{m_{cx}^p(x_0^p) m_{vx}^p(x_0^p)}{m_{cx}^p(x_0^p) + m_{vx}^p(x_0^p)}. \quad (B4d)$$

Also,

$$\frac{\partial f_{e/a}(0,0)}{\partial E_{\perp}} = \frac{1}{2} \int_{x_0^p}^{b_0} \sqrt{\frac{2m_{cx}^p(x')}{E_g \pm \hbar\omega - (E_{vx} - U(x'))}} dx' \quad (\text{B4e})$$

and

$$\frac{d^2 f_{e/a}(0,0)}{d\omega^2} = \frac{m_{cx}^p(x_0) + m_{vx}^p(x_0)}{\sqrt{2m_{rx_0}(E_g \pm \hbar\omega)}} \left[-\frac{dU}{dx} \right]_{x_0^p}. \quad (\text{B4f})$$

Finally, from eqs. (B2), (B3), (B4a) - (B4f), we get eq. (8). Note that the Gaussian integral over q_x converts the condition # into the condition * since $\int [M_{\mathbf{q},\mu}]_{\#} \exp(-\beta Q^2) dq_x \approx [M_{\mathbf{q},\mu}]_{*} \sqrt{\pi/\beta}$ by the method of steepest descent.

Appendix C: Multiplicity of tunneling paths

The conduction band minima in silicon are along the six equivalent $\langle 100 \rangle$ directions. As described in Ref. 22, the positions of these valleys are used to determine the values of \mathbf{k}^{\perp} to compute the complex bands $k^{\parallel}(E; \mathbf{k}^{\perp})$. The value $k^{\parallel}(E; \mathbf{k}^{\perp})$ represents the magnitude of the component of the wavevector, parallel or antiparallel to the transport direction, oriented along the direction of an arrow through the valley corresponding to \mathbf{k}^{\perp} , as shown in Fig. 5. Paths having the same $k^{\parallel}(E; \mathbf{k}^{\perp})$ are shown in the same color. Further, the paths shown solid in red have complex bands that enclose a smaller area $\int_{E_g} \text{Im}[k^{\parallel}(E)] dE$ bounded by the imaginary parts of the valence and conduction bands than those shown dashed in blue. It is necessary to consider valleys that lie on both sides of the $\mathbf{k}^{\parallel} = \mathbf{0}$ plane (shown shaded). Fig. 5 gives the multiplicity ν for the [100], [110] and [111] directions.

Appendix D: Transfer Matrix Method as an improvement over the WKB approximation

In order to use the transfer matrix method, we define points d_j , $j = 0, 1, \dots, N+1$ as shown in Fig. 6(a), so that the values of the wavevector are available at the midpoints of intervals $[d_j, d_{j+1}]$, $0 \leq j \leq N$. There are N interfaces ($1 \leq j \leq N$) between the classical turning points $x = a$ and $x = b_0$. For each of these interfaces, we have⁷ a transfer matrix $[M_j]$, given by

$$[M_j] = \frac{1}{2K_j m_{j+1}} \begin{bmatrix} C_j e^{\iota(K_{j+1} - K_j)d_j} & D_j e^{-\iota(K_{j+1} + K_j)d_j} \\ D_j e^{\iota(K_{j+1} + K_j)d_j} & C_j e^{-\iota(K_{j+1} - K_j)d_j} \end{bmatrix} \quad (\text{D1})$$

with $C_j = K_j m_{j+1} + K_{j+1} m_j$ and $D_j = K_j m_{j+1} - K_{j+1} m_j$. K_j is defined in Fig. 6(a); m_j is similarly evaluated from $m_{vx}(x)$ or $m_{cx}(x)$, based on whether the wavevector corresponds to the valence or conduction bands respectively. Note that $E_{cx} = E_{vx} \mp \hbar\omega$ for the

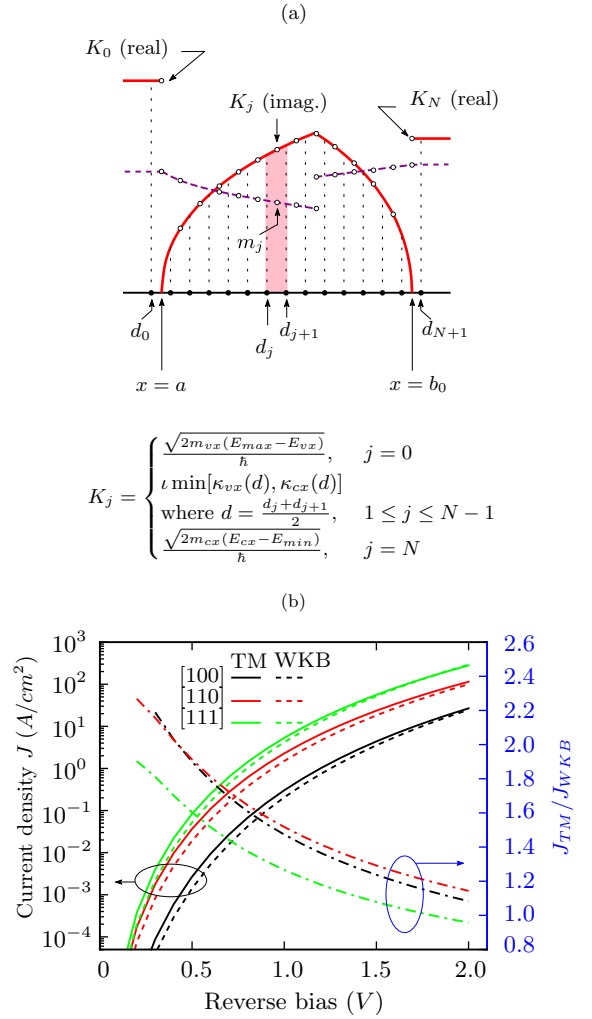


FIG. 6. (a) Description of the transfer matrix (TM) method. (b) Comparison of using the transfer matrix and WKB methods in the final expression for BTBT current for the devices described in eq. (8).

situation $Q_{e/a} = 0$, $E_{\perp} = 0$ described in eq. (B3). The transmission $T(E_{vx})$ is then

$$T(E_{vx}) = \frac{1}{|[M]_{1,1}|^2} \times \frac{k_{cx} - k_{0cx}}{k_{vx} - k_{0vx}} \frac{m_{vx}}{m_{cx}}, \quad \text{where} \quad (\text{D2a})$$

$$[M] = [M_1][M_2] \dots [M_N]. \quad (\text{D2b})$$

Also note that $K_0 \equiv k_{vx} - k_{0vx}$ and $K_N \equiv k_{cx} - k_{0cx}$ based on the assumption that the energy bands are flat outside the classical turning points.

A comparison of using the transfer matrix method to compute $T(E_{vx})$ instead of using the WKB result $T(E_{vx}) = e^{-\Lambda}$ in eq. (8) is shown in Fig. 6(b). The transfer matrix method predicts a higher current over most of the bias range.

ACKNOWLEDGMENT

A. Ajoy wishes to thank IBM India for financial support. The authors wish to thank Dr. Rajan Pandey (IBM Bangalore) and G. Vijayakumar (IIT Madras) for useful discussions.

- ¹C. Rivas, R. Lake, G. Klimeck, W. Frensley, M. Fischetti, P. Thompson, S. Rommel, and P. Berger, *Appl. Phys. Lett.* **78**, 814 (2001).
- ²M. Luisier and G. Klimeck, *J. Appl. Phys.* **107**, 084507 (2010).
- ³M. Luisier and G. Klimeck, in *International Conference on High Performance Computing, Networking, Storage and Analysis* (IEEE, 2008) pp. 1–10.
- ⁴M. Luisier and G. Klimeck, *Phys. Rev. B* **80**, 155430 (2009).
- ⁵M. Luisier, A. Schenk, W. Fichtner, and G. Klimeck, *Phys. Rev. B* **74**, 205323 (2006).
- ⁶G. A. M. Hurkx, *IEEE Trans. Electron Devices* **39**, 331 (1992).
- ⁷R. K. Pandey, K. V. R. M. Murali, S. S. Furkay, P. J. Oldiges, and E. J. Nowak, *IEEE Trans. Electron. Devices*, **57**, 2098 (2010).
- ⁸K.-H. Kao, A. S. Verhulst, W. G. Vandenberghe, B. Soree, G. Groeseneken, and K. De Meyer, *IEEE Trans. Electron Devices* **59**, 292 (2012).
- ⁹E. Kane, *J. Appl. Phys.* **32**, 83 (1961).
- ¹⁰S. Tanaka, *Solid State Electron.* **37**, 1543 (1994).
- ¹¹W. Vandenberghe, B. Sorée, W. Magnus, and M. Fischetti, *J. Appl. Phys.* **109**, 124503 (2011).
- ¹²A. Schenk, *Solid State Electron.* **36**, 19 (1993).
- ¹³L. Keldysh, *Soviet Journal of Experimental and Theoretical Physics* **6**, 763 (1958).
- ¹⁴W. Kohn, *Phys. Rev.* **115**, 809 (1959).
- ¹⁵V. Heine, *Proceedings of the Physical Society* **81**, 300 (1963).
- ¹⁶S. Laux, in *International Workshop on Computational Electronics* (IEEE, 2009) pp. 1–2.
- ¹⁷R. Tsu and L. Esaki, *Appl. Phys. Lett.* **22**, 562 (1973).
- ¹⁸P. Solomon, S. Laux, L. Shi, J. Cai, and W. Haensch, in *Device Research Conference 2009* (IEEE, 2009) pp. 263–264.
- ¹⁹S. E. Laux and P. M. Solomon, Unpublished.
- ²⁰M. Geller and W. Kohn, *Phys. Rev. Lett.* **70**, 3103 (1993).
- ²¹C. Huang, S. Chao, D. Hang, and Y. Lee, *Chin. J. Phys.* **46** (2008).
- ²²A. Ajoy, K. V. R. M. Murali, S. Karmalkar, and S. E. Laux, in *Device Research Conference, 2011* (IEEE, 2011) pp. 113–114.
- ²³A. Ajoy, K. V. R. M. Murali, and S. Karmalkar, *J. Phys.: Condens. Matter* **24**, 055504 (2012).
- ²⁴A. Rahman, M. S. Lundstrom, and A. W. Ghosh, *J. Appl. Phys.* **97**, 053702 (2005).
- ²⁵S. Tanaka, *Solid State Electron.* **38**, 683 (1995).
- ²⁶W. Vandenberghe, B. Sorée, W. Magnus, and G. Groeseneken, *J. Appl. Phys.* **107**, 054520 (2010).
- ²⁷A. Mayer, *Journal of Physics: Condensed Matter* **22**, 175007 (2010).
- ²⁸S. Chen, URL: <http://github.com/cogenda/pyEDA>.
- ²⁹M. Fischetti, T. O'Regan, S. Narayanan, C. Sachs, S. Jin, J. Kim, and Y. Zhang, *IEEE Trans. Electron. Devices* **54**, 2116 (2007).
- ³⁰T. B. Boykin, G. Klimeck, and F. Oyafuso, *Phys. Rev. B* **69**, 115201 (2004).
- ³¹H. C. Chen, S. S. Li, and K. W. Teng, *Solid State Electron.* **32**, 339 (1989).
- ³²J. Lowney, *Solid State Electron.* **28**, 187 (1985).
- ³³D. Miller, "Quantum Mechanics for Scientists and Engineers," (Cambridge University Press, 2008) Chap. 8, pp. 230–33.